A numerical model study of the main factors contributing to hypoxia and its interannual and intra-seasonal variability off the Changjiang Estuary

Haiyan Zhang[1, 2], Katja Fennel[1,*], Arnaud Laurent[1], Changwei Bian[3]

[1]Department of Oceanography, Dalhousie University, Halifax, Nova Scotia, Canada

[2]School of Marine Science and Technology, Tianjin University, Tianjin, China

[3] Physical Oceanography Laboratory/CIMST, Ocean University of China, and Qingdao National Laboratory for Marine Science and Technology, Qingdao, China

*Corresponding author

Abstract

A three-dimensional physical-biological model of the marginal seas of China was used to analyze interannual and intra-seasonal variations in hypoxic conditions and identify the main processes controlling their generation off the Changjiang Estuary. The model was validated against available observations and reproduces the observed temporal and spatial variability of physical and biological properties including bottom oxygen. Interannual variations of hypoxic extent are partly explained by variations in river discharge but not nutrient load. The spatial extent of the freshwater plume is a useful metric when relating riverine influences to biological rates and oxygen distributions. As riverine inputs of freshwater and nutrients are consistently high, promoting large productivity and subsequent oxygen consumption, wind forcing is important in modulating interannual and intra-seasonal variability. Wind direction is relevant because it determines the spatial extent and distribution of the freshwater plume which is strongly affected by either upwelling or downwelling conditions. High-wind events can lead to partial reoxygenation of bottom waters and, when occurring in succession throughout summer, can suppress the development of hypoxic conditions. An oxygen budget is presented and shows that sediment oxygen consumption is the dominant oxygen sink below the pycnocline and that advection of oxygen in the bottom waters acts as an oxygen sink in spring but becomes a

source during hypoxic conditions in summer especially in the southern part of the hypoxic region, which is influenced by open-ocean intrusions.

1. Introduction

In coastal seas, hypoxic conditions (oxygen concentrations lower than 2 mg L^{-1} or 62.5 mmol m^{-3}) are increasingly caused by rising anthropogenic nutrient loads from land (Diaz & Rosenberg, 2008; Rabalais et al., 2010; Fennel and Testa, 2019). Hypoxic conditions are detrimental to coastal ecosystems leading to a decrease in species diversity and rendering these systems less resilient (Baird et al., 2004; Bishop et al., 2006; Wu, 2002). Hypoxia is especially prevalent in coastal systems influenced by major rivers such as the northern Gulf of Mexico (Bianchi et al., 2010), Chesapeake Bay (Li et al., 2016), and the Changjiang Estuary (CE) in the East China Sea (Li et al., 2002).

The Changjiang River is the largest river in China and fifth largest in the world in terms of volume transport, with an annual discharge of 9×10^{11} m^3 $year^{-1}$ via its estuary (Liu et al., 2003). The mouth of the CE is at the confluence of the southeastward Yellow Sea Coastal Current and the northward Taiwan Warm Current (Figure 1). Hydrographic properties in the outflow region of the CE are influenced by several different water masses including fresh Changjiang Diluted Water, relatively low-salinity coastal water, more saline water from the Taiwan Warm Current, and high-nutrient, low-oxygen water from the subsurface of the Kuroshio (Wei et al., 2015; Yuan et al., 2008). The interactions of these water masses together with wind forcing and tidal effects lead to a complicated and dynamic environment.

Freshwater discharge reaches the minimum in winter when the strong northerly monsoon (dry season) prevails and peaks in summer during the weak southerly monsoon (wet season) resulting in a large freshwater (FW) plume adjacent to the estuary. Along with the FW, the Changjiang River delivers large quantities of nutrients to the East China Sea (ECS) resulting in eutrophication in the plume region (Li et al., 2014; Wang et al., 2016). Since the 1970s, nutrient load has increased more than twofold with a subsequent increase in primary production in the outflow region of the estuary (Liu et al., 2015). Hypoxia off the CE was first detected in 1959 and, with a spatial extent of up to 15,000 km^2, is among the largest coastal hypoxic zones in the world (Fennel & Testa, 2019). Although no conclusive

trend in oxygen minima has been observed (Wang, 2009; Zhu et al., 2011), hypoxic conditions are suspected to have expanded and intensified in recent decades (Li et al., 2011; Ning et al., 2011) due to the increasing nutrient loads from the Changjiang River (Liu et al., 2015).

It is generally accepted that water-column stratification and the decomposition of organic matter are the two essential factors for hypoxia generation, and this is also the case for the shelf region off the CE (Chen et al., 2007; Li et al., 2002; Wei et al., 2007). High solar radiation and freshwater input in summer contribute to strong vertical stratification which is further enhanced by near-bottom advection of waters with high salinities (> 34) and low temperatures (< 19 °C) by the Taiwan Warm Current. The resulting strong stratification inhibits vertical oxygen supply (Li et al., 2002; Wang, 2009; Wei et al., 2007). At the same time, high organic matter supply fuels microbial oxygen consumption in the subsurface (Li et al., 2002; Wang, 2009; Wei et al., 2007; Zhu et al., 2011). It has also been suggested that the TWC brings additional nutrients contributing to organic matter production (Ning et al., 2011) and that the low oxygen concentrations (~ 5 mg L^{-1}) of the TWC precondition the region to hypoxia (Ning et al., 2011; Wang, 2009).

While observational analyses suggest that hypoxia off the CE results from the interaction of various physical and biogeochemical processes, quantifying the relative importance of these processes and revealing the dynamic mechanisms underlying hypoxia development and variability require numerical modeling (Peña et al., 2010). Numerical modeling studies have proven useful for many other coastal hypoxic regions such as the Black Sea northwestern shelf (Capet et al., 2013), Chesapeake Bay (Li et al., 2016; Scully, 2013), and the northern Gulf of Mexico (Fennel et al., 2013; Laurent & Fennel, 2014).

Models have also been used to study the hypoxic region of the CE. Chen et al. (2015a) used a 3D circulation model with a highly simplified oxygen consumption parameterization (a constant consumption rate) to investigate the effects of physical processes, i.e. freshwater discharge, and wind speed and direction, on hypoxia formation. Chen et al. (2015b) examined the tidal modulation of hypoxia. The model domain in these two previous studies was relatively limited encompassing only the CE, Hangzhou Bay and the adjacent coastal ocean but did not cover the whole area affected by hypoxia (Wang, 2009; Zhu et al., 2011). Zheng et al. (2016) employed a nitrogen cycle model coupled with a 3D

hydrodynamic model to examine the role of river discharge, wind speed and direction on hypoxia, and also emphasized the physical controls. These previous modeling studies focused on the response of hypoxia to physical factors only and did not address seasonal evolution and interannual variations of hypoxia or the influence of variability in biological rates.

More recently, Zhou et al. (2017) analyzed the seasonal evolution of hypoxia and the importance of the Taiwan Warm Current and Kuroshio intrusions as a nutrient source using an advanced coupled hydrodynamic-biological model. However, the baseline of their model does not include sediment oxygen consumption (SOC), which is thought to be a major oxygen sink in the hypoxic region off the CE (Zhang et al., 2017) and other river-dominated hypoxic regions including the northern Gulf of Mexico (Fennel et al. 2013, Yu et al. 2015a,b). Zhou et al. (2017) acknowledged the importance of SOC based on results from a sensitivity experiment but did not quantify its role in hypoxia generation.

Here we introduce a new 3D physical-biological model implementation for the ECS that explicitly includes nitrogen and phosphorus cycling and SOC. The model is a new regional implementation for the ECS of an existing physical-biogeochemical model framework that has been extensively used and validated for the northern Gulf of Mexico (Fennel et al., 2011, 2013; Laurent et al., 2012; Laurent and Fennel, 2014; Yu et al., 2015b; Fennel and Laurent, 2018). The hypoxic zones in northern Gulf of Mexico and off the CE have similar features including the dominant influence of a major river (Changjiang and Mississippi), a seasonal recurrence every summer, a typical maximum size of about 15,000 km^2, documented P-limitation following the major annual discharge in spring and a significant contribution of SOC to oxygen sinks in the hypoxic zone (Fennel and Testa 2019). Here the model is used to explore the evolution of hypoxia on interannual and intra-seasonal scales and to identify the main factors contributing to the different modes of variability. For this study, we performed and validated a 6-year simulation in the ECS, discuss the main drivers of interannual and intra-seasonal variability, and present an oxygen budget to quantify the relative importance of SOC and the influence of lateral advection of oxygen. A companion study by Grosse et al. (2020) uses the same model to quantify the importance of intrusions of nutrient-rich oceanic water from the Kuroshio for hypoxia development off the CE.

2. Model description

2.1. Physical model

The physical model used in this study is based on the Regional Ocean Modeling System (ROMS; Haidvogel et al., 2008) and was implemented for the ECS by Bian et al. (2013a). The model domain extends from 116°E to 134°E and from 20°N to 42°N (Figure 1), covering the Bohai Sea, the Yellow Sea, the ECS, part of the Japan Sea and the adjacent northwest Pacific, with a horizontal resolution of 1/12° (about 10 km) and 30 vertical layers with enhanced resolution near the surface and bottom. The model uses the recursive Multidimensional Positive Definite Advection Transport Algorithm (MPDATA) for the advection of tracers (Smolarkiewicz and Margolin, 1998), a third-order upstream advection of momentum, and the Generic Length Scale (GLS) turbulence closure scheme (Umlauf & Burchard, 2003) for vertical mixing.

The model is initialized with climatological temperature and salinity from the World Ocean Atlas 2013 V2 (WOA13 V2) (Locarnini et al., 2013; Zweng et al., 2013), and is forced by 6-hourly wind stress, and heat and freshwater fluxes from the ECMWF ERA-Interim dataset (Dee et al., 2011). Open boundary conditions for temperature and salinity are prescribed from the monthly climatology (WOA13 V2), and horizontal velocities and sea surface elevation at the boundaries are specified from the monthly SODA data set (Carton & Giese, 2008). In addition, eight tidal constituents (M2, S2, N2, K2, K1, O1, P1 and Q1) are imposed based on tidal elevations and currents are extracted from the global inverse tide model data set of TPXO7.2 of Oregon State University (OSU, Egbert & Erofeeva, 2002). At the open boundaries, Chapman and Flather conditions are used for the free surface and the barotropic velocity, respectively, and the radiation condition for the baroclinic velocity. Eleven rivers are included in the model. Freshwater discharge from the Changjiang River uses daily observations from the Datong Hydrological Station (DHS; www.cjh.com.cn). Since daily observations are not available for the other rivers, we prescribed monthly or annual climatologies (Liu et al., 2009; Tong et al., 2015; Zhang, 1996).

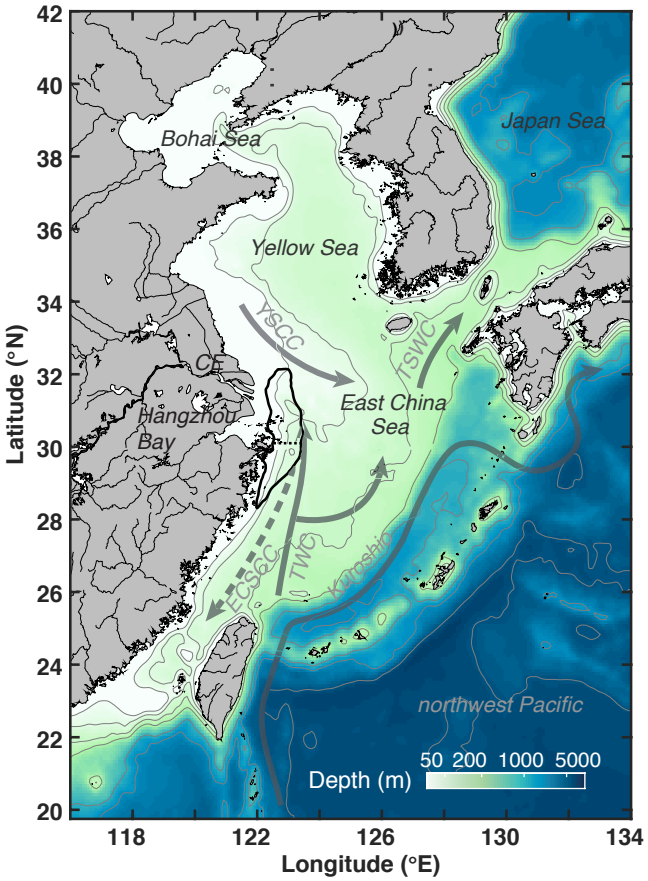

Figure 1. Bathymetry of the model domain with 30, 50, 100, 200, 1000, 2000 and 5000 m isobaths. The black outline near the Changjiang Estuary (CE) and Hangzhou Bay indicates the zone typically affected by low-oxygen conditions (dotted line shows separation between northern and southern zones). Solid grey arrows denote currents present throughout the year (Kuroshio; TWC: Taiwan Warm Current; YSCC: Yellow Sea Coastal Current). The dashed grey arrow indicates the direction of the wintertime East China Sea Coastal Current (ECSCC) which flows in the opposite direction to summertime flow.

2.2. Biological model

The biological component is based on the pelagic nitrogen cycle model of Fennel et al. (2006, 2011, 2013) and was extended to include phosphate (Laurent et al., 2012; Laurent & Fennel, 2014) and riverine dissolved organic matter (Yu et al., 2015b). The model includes two forms of dissolved inorganic nitrogen (DIN), nitrate (NO3) and ammonium (NH4), phosphate (PO4), phytoplankton (Phy), chlorophyll (Chl), zooplankton (Zoo), two pools of detritus, suspended and slow-sinking small detritus (SDet) and fast-sinking large

detritus (LDet), and riverine dissolved organic matter (RDOM). Here, riverine dissolved and particulate organic nitrogen enter the pools of RDOM and SDet, respectively. The remineralization rate of RDOM is an order of magnitude lower than that of SDet to account for the more refractory nature of the riverine dissolved organic matter (Yu et al., 2015b).

At the sediment-water interface, SOC is parameterized assuming "instantaneous remineralization," i.e. all organic matter reaching the sediment is remineralized instantaneously and oxygen is consumed due to nitrification and aerobic remineralization at the same time. In the "instantaneous remineralization", all phosphorus is returned to the water column as PO4 while a constant fraction of fixed nitrogen is lost due to denitrification. All biogeochemical model parameters are given in Table S1 in the Supplement. A more detailed model descriptions can be found in the Supplement to Laurent et al. (2017).

Light is vertically attenuated by chlorophyll, detritus and seawater itself. In addition, to account for the effects of colored dissolved organic matter (CDOM) and suspended sediments, which show relatively high values near the coast and in the river plume (Bian et al., 2013b; Chen et al., 2014), a light-attenuation term dependent on water depth and salinity is introduced which yields higher attenuation in shallow areas and in the FW plume.

Initial and boundary conditions for NO3, PO4 and oxygen are prescribed using the World Ocean Atlas 2013 (WOA13) climatology (Garcia et al., 2013a,b). A small positive value is used for the other variables. NO3 is nudged towards climatology in the northwest Pacific at depth > 200 m. Monthly nutrient loads of NO3 and PO4 from the Changjiang are from the Global-NEWs Model (Wang et al., 2015) but were adjusted by multiplicative factors of 1.20 and 1.66, respectively, to ensure a match between simulated and observed nutrient concentrations in the CE (see July and Aug 2012 in Figure 2). Nutrient loads in other rivers are based other published climatologies (Liu et al., 2009; Tong et al., 2015; Zhang, 1996).

We performed an 8-year simulation from 1 January 2006 to 31 December 2013, with 2006-2007 as model spin up and 2008-2013 used for analysis. Model output was saved daily.

3. Results

3.1. Model validation

The model is validated by comparing simulated surface and bottom temperature, salinity, current patterns and strengths, surface chlorophyll, surface nitrate and bottom oxygen to observations. The model reproduces remotely sensed spatial and temporal SST patterns (NOAA AVHRR) very well with an annual correlation coefficient of 0.98 (Figure S1). Simulated surface and bottom salinity also show similar spatial and seasonal patterns as available *in situ* observations (Figures S2 and S3) with correlation coefficients of 0.77 and 0.84, respectively. Simulated surface and bottom temperature, when compared with available *in situ* data (Figures S4 and S5), are also consistent with the observations with correlation coefficients of 0.96 and 0.93.

The simulated current systems in the ECS and YS show typical seasonal variations as follows (see also Figure S6). In winter, currents mainly flow southward on the Yellow Sea and ECS shelves driven by the northerly wind. In contrast, the East China Sea Coastal Current and the Korean Coastal Current flow northward in summer. The Kuroshio is

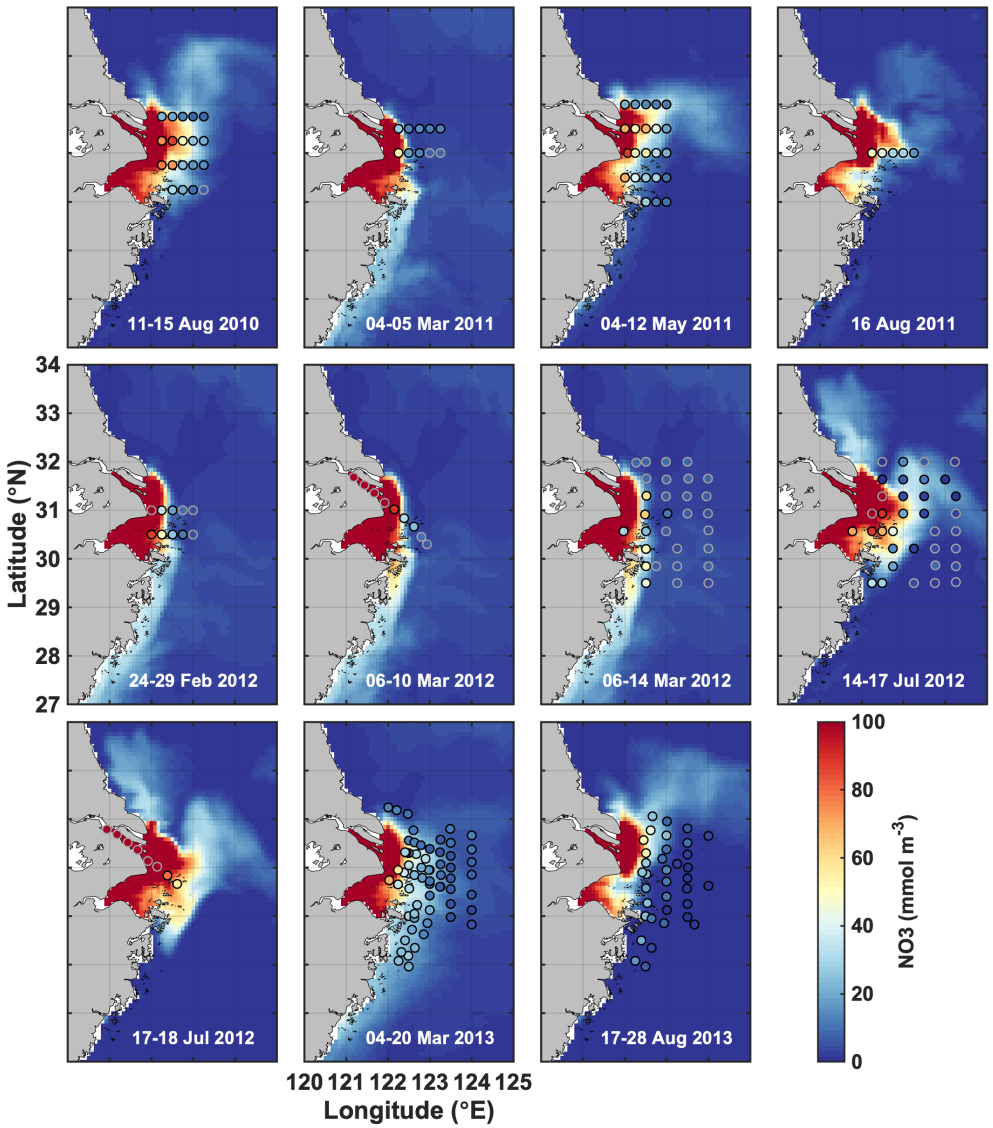

Figure 2: Simulated surface nitrate (colored map) shown for the day that marks the mid-point of the cruise dates (given in each panel) the compared to observations (dots) during 11 cruises from 2011 to 2013.

stronger in summer than in winter. The model captures the seasonal pattern of the current system and resolves currents in the ECS and Yellow Sea (also see Grosse et al. 2020).

Simulated monthly averaged (2008-2013) surface chlorophyll concentrations in May, August and November are compared with satellite-derived fields (MODIS-Terra) and agree well with correlation coefficients of 0.77, 0.94 and 0.64, respectively (Figure S7).

Simulated surface nitrate concentrations are shown in comparison to in situ observations in Figure 2 and agree well with a correlation coefficient of 0.84. Observations in March

and July of 2012 show strongly elevated concentrations in the CE and a sharp gradient in the vicinity of the estuary's mouth that are well represented by the model. Likewise, simulated and observed bottom oxygen distributions are compared in Figure 3 and agree reasonably well overall with a correlation coefficient of 0.71 although the model underestimates observed low-oxygen conditions in July of 2011 and 2013 and August 2013.

Together, these comparisons show that the model is able to reproduce important aspects of the physical-biogeochemical dynamics in the study region.

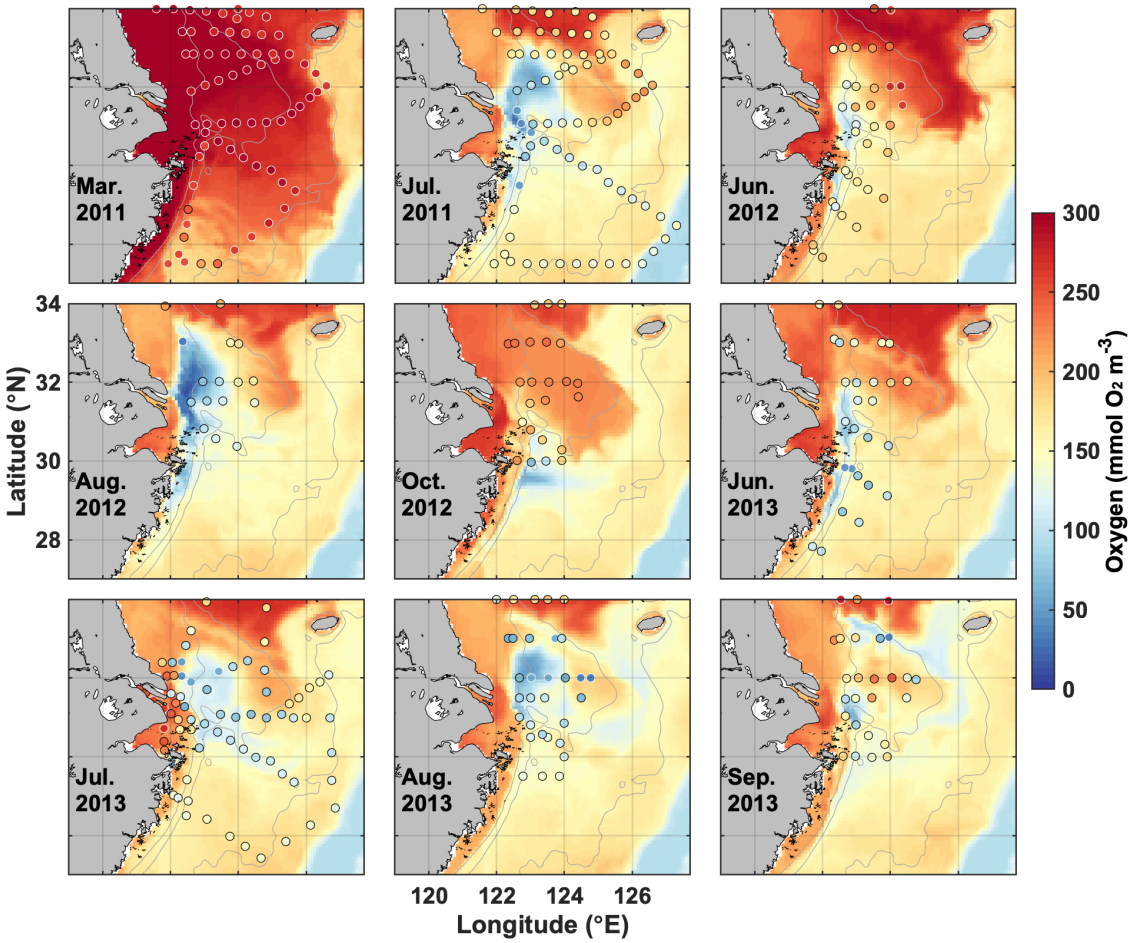

Figure 3. Simulated bottom oxygen (colored map) shown for the day that marks the mid-point of the cruise dates compared with observations (dots) during nine cruises from 2011 to 2013.

3.2. Simulated oxygen dynamics

The model simulates annually recurring hypoxic conditions with a typical seasonal cycle where bottom waters are well-oxygenated until April/May, hypoxic conditions establish in June or July, become more pronounced in August, and disperse in October or November (Figure 4a, c). However, the model also simulates significant interannual variability in timing and extent of hypoxia over the 6-year simulation period (Figure 4b, c). The years with largest maximum hypoxic extent are 2010 (20,520 km^2), 2009 (16,660 km^2), 2012 (13,930 km^2) and 2008 (12,720 km^2) while the simulated hypoxic extent is much smaller (<5,000 km^2) in 2011 and 2013. The ranking is similar when considering the time-integrated hypoxic extent (Figure 4b). The year with the largest maximum and integrated hypoxic extent (2010) also has the highest peak discharge (Figure 4a) and highest annual

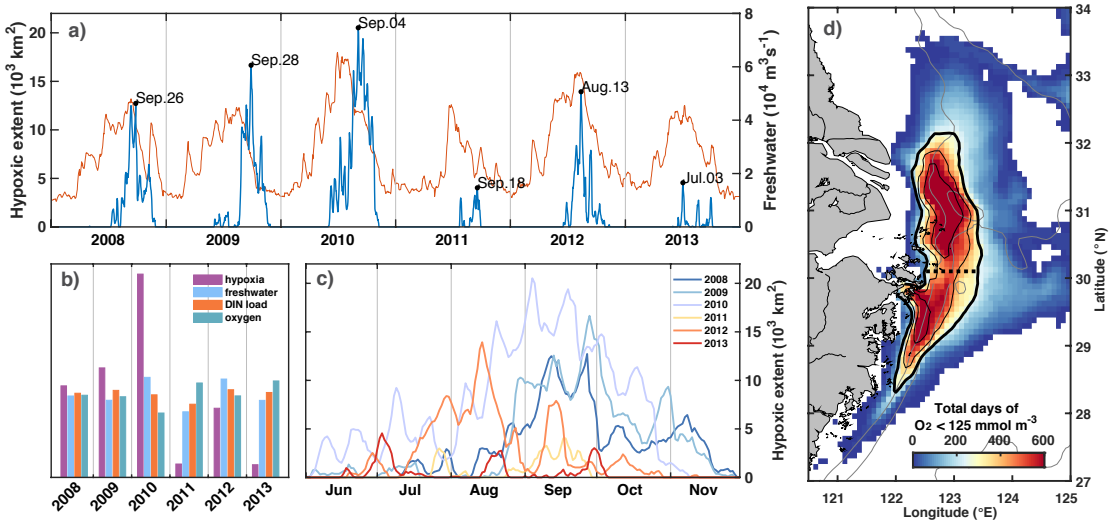

Figure 4. a) Time series of freshwater discharge and simulated hypoxic extent with peaks specified by date. b) Annual comparison of normalized time-integrated hypoxic extent, freshwater discharge, and DIN load, and summer-mean bottom oxygen concentration. c) Evolution of simulated hypoxic extent by year. d) Frequency map of number of days when bottom oxygen concentrations were below 125 mmol m^{-3} (4 mg/l). The black isolines indicate 240, 360 and 480 days (or 40, 60 and 80 days per year). The thick solid line indicates the region we refer to as the typical low-oxygen zone and the dashed line shows the demarcation between its northern and southern regions.

242 freshwater discharge (65,400 m^3 s^{-1}), although the annual discharge is similar to 2008 and
243 2012.
244 The region where low-oxygen conditions are most commonly simulated is indicated by the
245 frequency map in Figure 4d, which shows the total number of days in the 6-year simulation
246 when bottom oxygen concentrations were below 125 mmol m^{-3} (or 4 mg/l), i.e. twice the
247 hypoxic threshold. It is known from observations that there are two centers of recurring
248 hypoxic conditions: the northern core is located just to the east of the CE and Hangzhou
249 Bay and the southern core to the southeast of Hangzhou Bay. The model is consistent with
250 these observations and simulates two distinct core regions of low-oxygen conditions
251 centered at 31°N and 29.3°N. The northern core region is larger than the southern core
252 region (9,050 km^2 for a threshold of 80 days per year of < 4 mg/l compared to 5,230 km^2).
253 We will refer to the region defined by a threshold of 40 days of < 4 mg/l of per year (solid
254 black line in Figure 1 and 4d) as the "typical low-oxygen zone" for the remainder of the
255 manuscript and demarcate the northern and southern sections by 30.1°N latitude (dashed
256 line in Figures 1 and 4d).
257 There are marked differences in the phenology of simulated hypoxic extent (Figure 4c).
258 Among the four years with largest hypoxic areas, hypoxia establishes relatively late (mid-
259 August) and lasts long (into November) in 2008 and 2009. In contrast in 2012, hypoxic
260 conditions establish earlier (June), are most pronounced in August and are eroded by mid-
261 October. In 2010, the year with the largest peak extent, hypoxia establishes already at the
262 beginning of June and is maintained until the end of October, leading to the by far largest
263 time-integrated hypoxia among the 6 years (Figure 4b). In all years there are times when
264 hypoxic extent decreases rapidly. In the following sections we explore the drivers of
265 interannual and intra-seasonal variations in low-oxygen conditions and the role of
266 biological processes and physical forcing.
267
268 *3.2.1 Interannual variations in hypoxia*
269 As mentioned above, there is significant interannual variation in hypoxic extent in the 6-
270 year simulation (Figure 4a, b, c). The years with the largest time-integrated hypoxic events
271 are 2010, 2009 and 2008 followed by 2012 with the fourth largest hypoxic extent. In 2011
272 and 2013, hypoxic conditions were much less severe than in the other 4 years. Freshwater

(FW) input and nutrient load are less variable with the largest FW inputs in 2010 and 2012 and the lowest in 2011. In an attempt to explain the interannual variations in hypoxia, we consider first the role of riverine FW inputs and nutrient loads. More specifically, we investigate correlations of time-integrated hypoxic area, average primary production (PP), total oxygen consumption (OC) by respiration, sediment oxygen consumption (SOC) and bottom oxygen in the typical low-oxygen zone, and the spatial extent of the FW plume with annually integrated FW input and DIN load (Figure 5).

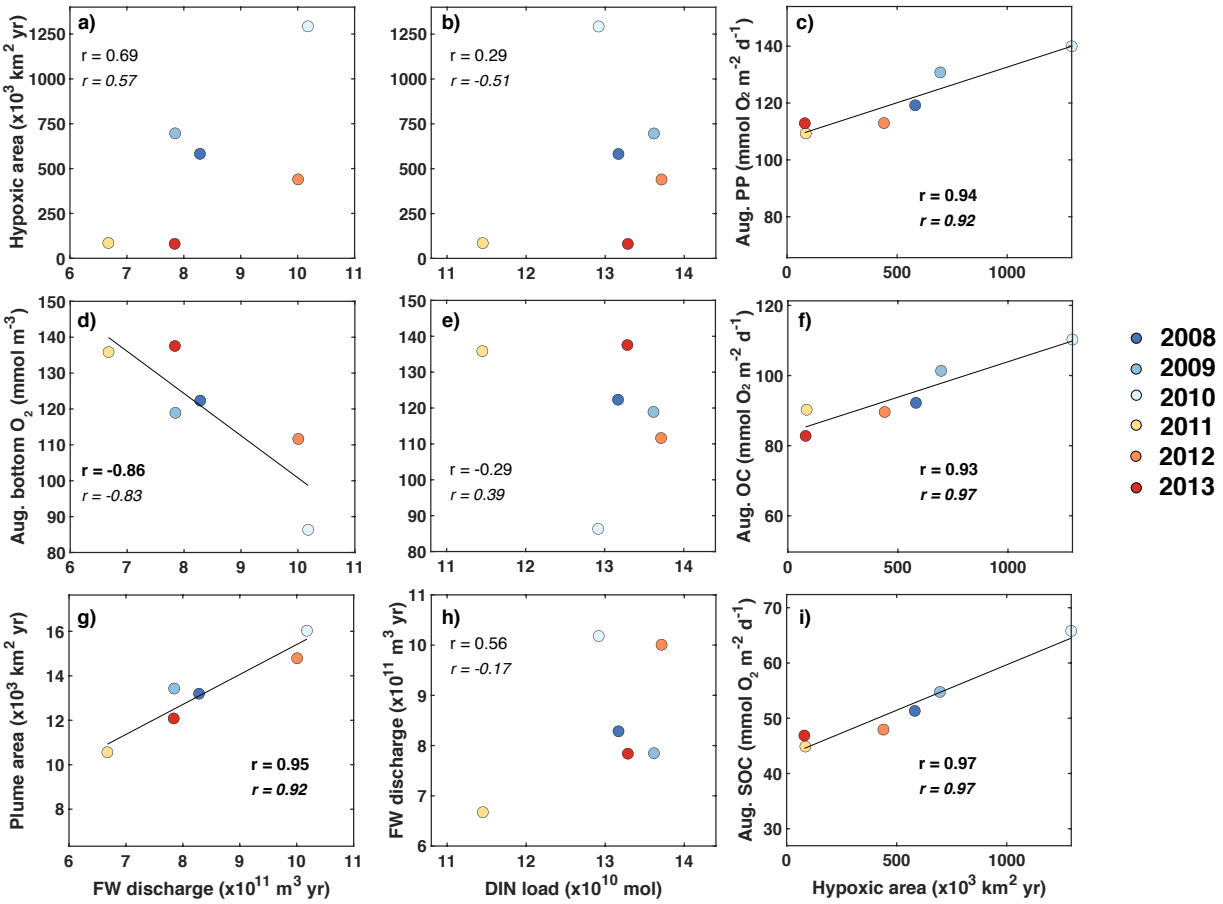

Figure 5. Correlations of time-integrated hypoxic area, average primary production, respiration and bottom oxygen in the typical low-oxygen zone in August, and the spatial extent of the FW plume (defined here as the area with surface salinity smaller than 25) with annually integrated FW input and DIN load. Correlation coefficients are given for all 6 years and, in italic font, after excluding year 2011. Significant correlations are shown in bold font and linear regressions indicated by the black line whenever the correlation is significant at $p<0.05$.

There is a significant negative correlation between annual FW input and mean bottom-water oxygen concentration in the low-oxygen zone of -86% and a weaker, statistically insignificant positive correlation of 69% between annual FW input and integrated hypoxic area (Figure 5a, d). This indicates that variations in FW input at least partly explain variability in hypoxic conditions. Perhaps surprisingly, there is no convincing correlation between annual FW input and annual DIN load (Figure 4h). Although the correlation coefficient is 56% when all 6 years are considered, the correlation drops to -17% when the low-flow year 2011 is excluded and neither of these correlations is statistically significant. As expected, there is a strong positive correlation of 95% between annual FW input and time-integrated plume area (Figure 4g). Plume area can thus be interpreted as a proxy of FW input.

In contrast to the positive correlations between FW input and hypoxia as well as bottom oxygen, correlations between the annual DIN load and integrated hypoxic area as well as mean bottom-water oxygen are much weaker and insignificant (Figure 4b, e). This implies that interannual variations in DIN load do not explain year-to-year variations in hypoxia. However, the correlations between integrated hypoxic area and mean rates of PP and OC (especially SOC) in August are significant and strong at 94% and 93% (97%), respectively (Figure 5c, f, i). The high correlation between hypoxic area and OC is primarily driven by SOC. Clearly, biological processes are important drivers of hypoxia and contribute to its interannual variability, but they do not appear to result from variations in DIN load. More relevant are variations in FW load, which explain interannual variations in hypoxia at least partly.

Clearly, other factors than riverine inputs must be at play in driving interannual variations. For example, comparing the years 2010 and 2012, both had very similar FW input and DIN load, but differed in severity of hypoxia (Figure 5a, b). Likewise, the years 2009 and 2013 were very similar in terms of FW input and DIN load, but very different in hypoxic extent. Next, we investigate the role of biological and physical drivers of intra-seasonal and interannual variability in hypoxia.

3.2.2 Biological drivers of intra-seasonal variability in hypoxia

In order to explore whether biological rates are related to the presence of FW, and whether the correlations that emerged when relating mean annual quantities also hold on shorter time scales, it seems prudent to distinguish between the northern and southern regions. The bathymetry in the northern zone is slightly deeper than in the southern zone (median depth of 28.5 m versus 24.6 m) and several biological rates with direct relevance to oxygen dynamics are different between the two zones (Figure 6). During the summer months (June to September), primary production (PP), oxygen consumption in the water column (WOC=OC-SOC), and SOC are larger in the northern zone with medians of 124 compared to 77.0 mmol O_2 m^{-2} d^{-1} for PP, of 43.1 versus 35.9 mmol O_2 m^{-2} d^{-1} for WOC, and 49.3 versus 27.3 mmol O_2 m^{-2} d^{-1} for SOC. During hypoxic conditions, PP and SOC are also notably larger in the northern zone with medians of 151 versus 107 mmol O_2 m^{-2} d^{-1} for PP and 69.9 versus 50.4 mmol O_2 m^{-2} d^{-1} for SOC. In the water column, the difference is reversed and WOC larger in the southern than the northern zone (52.9 versus 46.7 mmol O_2 m^{-2} d^{-1}). Because of these different characteristics, we consider the northern and southern zones of the typical low-oxygen region separately.

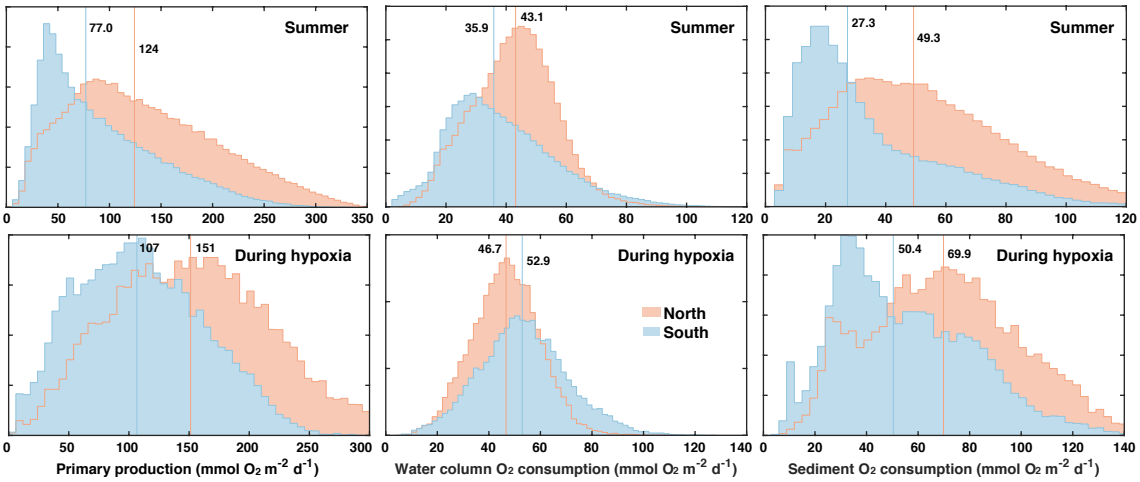

Figure 6: Histograms primary production and water-column and sediment respiration during the summer months (June to September) and during hypoxic conditions in the northern and southern parts of the typically hypoxic zone. Medians are indicated by vertical lines.

The annual correlations presented in the previous section indicate that biological rates are important drivers for interannual variability but not due to variations in nutrient load.

Variability in annual FW input is a better predictor. In order to better understand how variability in FW is related to biological rates and thus hypoxia, we first explore whether significant relationships exist between daily biological rates, bottom-water oxygen, and the presence of FW in the two zones. Since annual FW input is highly correlated with the extent of the FW plume (see Figure 5g), daily plume extent can be used as a measure of FW presence and compared to daily rates of PP, OC, SOC, and bottom oxygen.

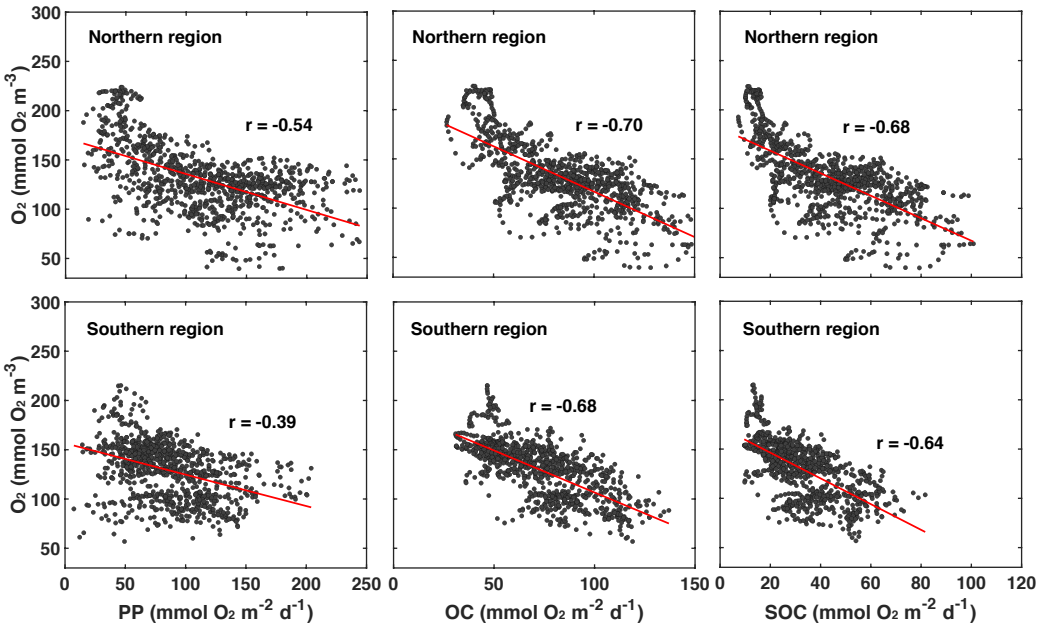

Figure 7. Correlations of daily averaged rates of PP, OC and SOC plotted with daily mean bottom oxygen concentration in the northern and southern regions of the low-oxygen zone in summer. The correlations are all significant. Correlation coefficients and slope and intercept of linear regressions (indicated by red lines) are given in Table 1.

Relationships between bottom oxygen (mmol m^{-3}) in northern region and											
PP (mmol O_2 m^{-2} d^{-1})			OC (mmol O_2 m^{-2} d^{-1})			SOC (mmol O_2 m^{-2} d^{-1})					
r	a	b	r	a	b	r	a	b			
-0.54	-0.36	172	-0.70	-0.92	209	-0.68	-1.14	181			
Same for the southern region											
-0.39	-0.32	157	-0.68	-0.85	192	-0.64	-1.30	172			
Relationships between plume area (10^3 km^2; defined by surface salinity < 29) in northern region and											
PP (mmol O_2 m^{-2} d^{-1})			OC (mmol O_2 m^{-2} d^{-1})			SOC (mmol O_2 m^{-2} d^{-1})			Bottom oxygen (mmol m^{-3})		
0.62	6.04	47.6	0.49	2.48	57.7	0.51	2.05	22.0	-0.56	-3.74	171
Same for the southern region											
0.43	3.78	64.6	0.56	3.18	57.8	0.43	1.50	24.7	-0.49	-3.52	149

Table 1. Correlation coefficients and parameters of a linear model fit (of the form y=ax+b) between

Daily PP, OC, and SOC are all significantly and negatively correlated with bottom-water oxygen (Figure 7, Table 1). This confirms that local production of organic matter and the resulting biological oxygen consumption are important for hypoxia development. However, it is also obvious that variability around the best fit is large (Figure 7). Furthermore, bottom oxygen and biological rates are significantly correlated with the extent of the FW plume (Table 1). This suggests that variability in the presence of FW contributes to variability in hypoxia not only by increasing vertical stratification and thus inhibiting vertical supply of oxygen to the subsurface but also because PP and respiration is larger in the river plume. Likely, large FW plumes stimulate more widespread biological production and thus oxygen consumption.

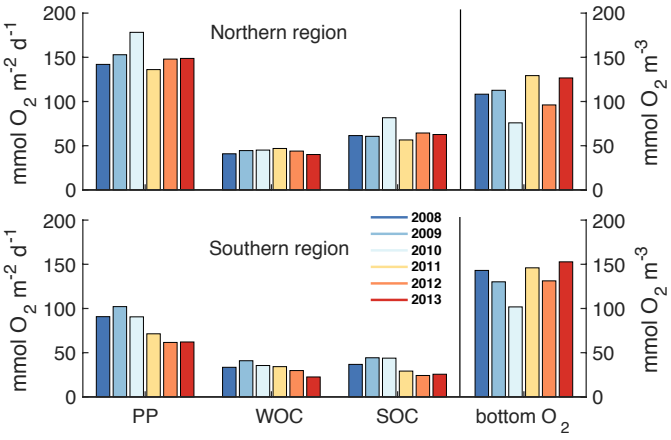

Figure 8. Mean August rates of PP, WOC, and SOC and mean bottom oxygen concentration in the northern and southern regions for 6-year simulation.

However, variations in biological rates alone do not explain variability in bottom oxygen concentrations and hypoxia. In Figure 8, we show August mean rates of PP, WOC, and SOC as well as mean bottom oxygen in the northern and southern zones for all years. In the northern zone, WOC is remarkably similar in all years. PP and SOC are also similar except in 2010 when SOC is higher. The low bottom oxygen concentration in 2010 could be explained by the relatively higher SOC; however, 2012 also had relatively low bottom oxygen while biological rates were similar to the other years with higher bottom oxygen. Likewise in the southern zone, differences in PP, WOC, and SOC among the years do not explain differences in bottom oxygen, as the years with the lowest bottom oxygen (2010

and 2012) are not the years with the highest PP and oxygen consumption rates. Next, we analyse the role of wind forcing, direction and stratification.

3.2.3 Physical drivers of intra-seasonal variability in hypoxia

We focus our analysis of physical drivers on wind direction and wind strength and their relation to FW plume location and extent because the latter has already been identified as an explanatory variable for interannual variations.

Wind direction is relevant because for most of June, July, and August winds blow predominantly from the south, but switch to predominantly northerly winds between the 2nd half of August and the end of September. As a result of the northward, upwelling favorable winds in the early summer, the FW plume is spread offshore and overlaps primarily with the northern zone. After the switch to mostly southward, downwelling-favorable directions, the FW plume moves southward, becomes more contained near the coast, and grows in its southward extent as it is transported by a coastal current. Wind direction has a demonstrable impact on PP and the extent of the FW plume as shown in Figure 9 for the month of September. Especially in the region, PP and plume extent are notably larger during southerly winds when the FW plume is more spread out, than during northerly winds when the plume is restricted to the coastal current.

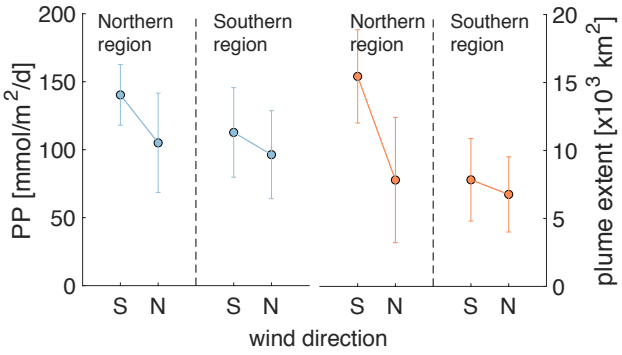

Figure 9. Mean PP and FW plume extent in the northern and southern regions averaged over days with north and south wind (i.e. when direction is +/- 45˚ of true north or south) and wind strength >0.03 Pa for in September.

Wind strength is relevant because storm events can erode vertical stratification and thus lead to resupply of oxygen to bottom waters due to vertical mixing. We investigated the effect of wind strength on bottom oxygen, hypoxia, and the extent of the FW plume by first inspecting time series of these variables (Figure S8). We isolated all event during the months June to September and, in Figure 10, show the corresponding changes in wind stress, mean bottom oxygen in the northern and southern zones, and the extent of the FW plume. We diagnosed these events as follows. First, we identified all days when the wind stress exceeded 0.12 Pa. Then we detected the minima in wind stress adjacent to the high-wind days by searching for minima in wind stress within 3 days prior and 3 days after the high-wind days. The periods within these minima are used as analysis period for each wind event. In four instances the wind stress exceeded the threshold within 5 days of a previous wind event. Those subsequent high-wind events were combined into one. We identified the minimum in bottom oxygen (maximum in FW plume area) at the beginning of the event and the maximum in oxygen (minimum in FW area) after the maximum in wind stress was reached.

Figure 10a illustrates rapid increases in wind stress typically within 2 to 4 days. The only exceptions are the 4 events where two storms occurred in rapid succession and the combined event lasted longer (up to 8 days) until maximum wind stress was reached. The year with the most wind events is 2013 (with 8 in total including one of the combined long-lasting event). The year with the least events is 2010 (2 events) followed by 2009 (3 events). Most of these events resulted in notable increases in mean bottom oxygen, typically by 10 to 30 mmol m^{-3}, but up to 100 mmol m^{-3} in 2010 in the southern zone (Figure 10b). In the rare cases where bottom oxygen did not increase or slightly decreased, bottom oxygen was already elevated before the wind event. The wind events strongly affected the extent of the FW plume (Figure 10c) by mixing the freshwater layer with underlying ocean water. The effects are largest when the FW plume was most expansive. This analysis shows the significant role of storm events in disrupting the generation of low-oxygen conditions and ventilating bottom waters.

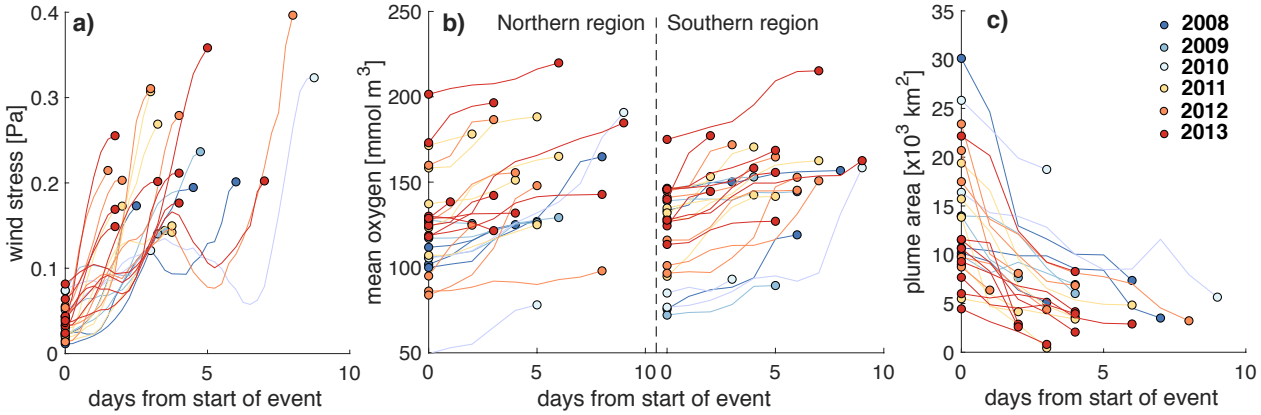

Figure 10. Evolution of a) wind stress, b) bottom mean oxygen in the northern and southern regions, and c) extent of the FW plume during high-wind events. These events are defined by wind stress exceeding 0.12 Pa.

In section 3.2.1 above, we noted that while the years 2010 and 2012 had very similar FW input and DIN load, 2010 had a much larger hypoxic area. Likewise, the years 2009 and 2013 were very similar in terms of FW input and DIN load, but 2009 had a much larger hypoxic area. Considering the frequency and severity of high-wind events explains the differences in both cases.

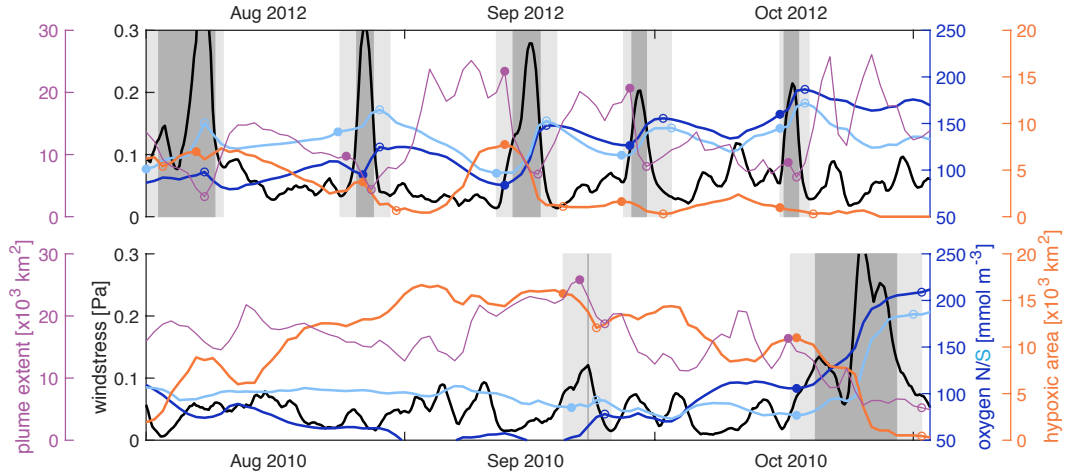

Figure 11. Wind stress (black), mean bottom oxygen in the northern and southern zones (dark and light blue), total hypoxic extent (orange), and FW plume extent (purple) throughout August, September and October of 2010 and 2012. The filled and open circles indicate a variables' value at

439 the beginning and after high-wind events. High-wind days/events are indicated by the dark/light
440 gray shading.

441 Figure 11 shows the wind stress, mean bottom oxygen in the northern and southern
442 zones, and total hypoxic extent and FW plume extent in 2012 and 2010. In 2012, there
443 were 5 high-wind events during the months of August, September, and October that all
444 coincided with increases in bottom oxygen, decreases in hypoxic extent when a hypoxic
445 zone was established at the beginning of the event, and decreases in FW plume extent.
446 Inspection of the evolution of bottom oxygen is especially instructive. While bottom
447 oxygen concentrations declined during periods with average or low wind, they were
448 essentially resent at a much higher level during each wind event. Whenever the FW plume
449 was extensive at the beginning of a high-wind event, it was drastically reduced during the
450 event. In 2010 bottom oxygen was at similar levels to 2012 at the beginning of August but
451 dropped to low levels throughout August, especially in the northern zone, and remained
452 low with widespread hypoxia until a major wind event in the second half of October
453 ventilated bottom waters. Except for a very short event in the second half of September,
454 there were no high-wind events from August until mid-October in 2010.

455 The differences in hypoxia in 2009 and 2013 can also be explained by the frequency
456 and intensity of high-wind events. In 2013, there were 8 high-wind events from July to
457 October that led to an almost continuous ventilation of bottom waters while in 2009 there
458 were only 3 such events during the same period (Figure S8). Low to average winds from
459 mid-August to early October of 2009 coincided with a decline in bottom oxygen and
460 establishment of an expansive hypoxic zone throughout most of September.

461 These analyses show that wind direction and strength play an important role in
462 determining the location of the hypoxic zone (i.e. northern versus southern region) and the
463 extent and severity of hypoxic conditions.

464

465 ***3.3 Oxygen budgets for the northern and southern regions***

466 In order to further investigate the roles of physical and biological processes in regulating
467 hypoxia, oxygen budgets are calculated from daily model output for the period from March
468 to August for the northern and southern hypoxic regions. Considering that hypoxic
469 conditions occur near the bottom, we evaluate an oxygen budget not only for the whole

water column but also for its lower portion which typically becomes hypoxic. To account for variations in the thickness of the hypoxic layer, which tends to be thicker in deeper waters (similar to observations by Ning et al., 2011), we include the bottommost 12 layers of our model grid. Because of the model's terrain-following vertical coordinates, the thickness of these 12 model layers varies with total depth as shown. The terms considered in the budget are air-sea flux, lateral physical advection and diffusion, vertical turbulent diffusion (for the subsurface budget only), PP, WOC (including respiration and nitrification), and SOC. Each term is integrated vertically over the whole water column and also over the bottom-most 12 layers and then averaged for the northern and southern regions for each month (Figure 12, Table S2).

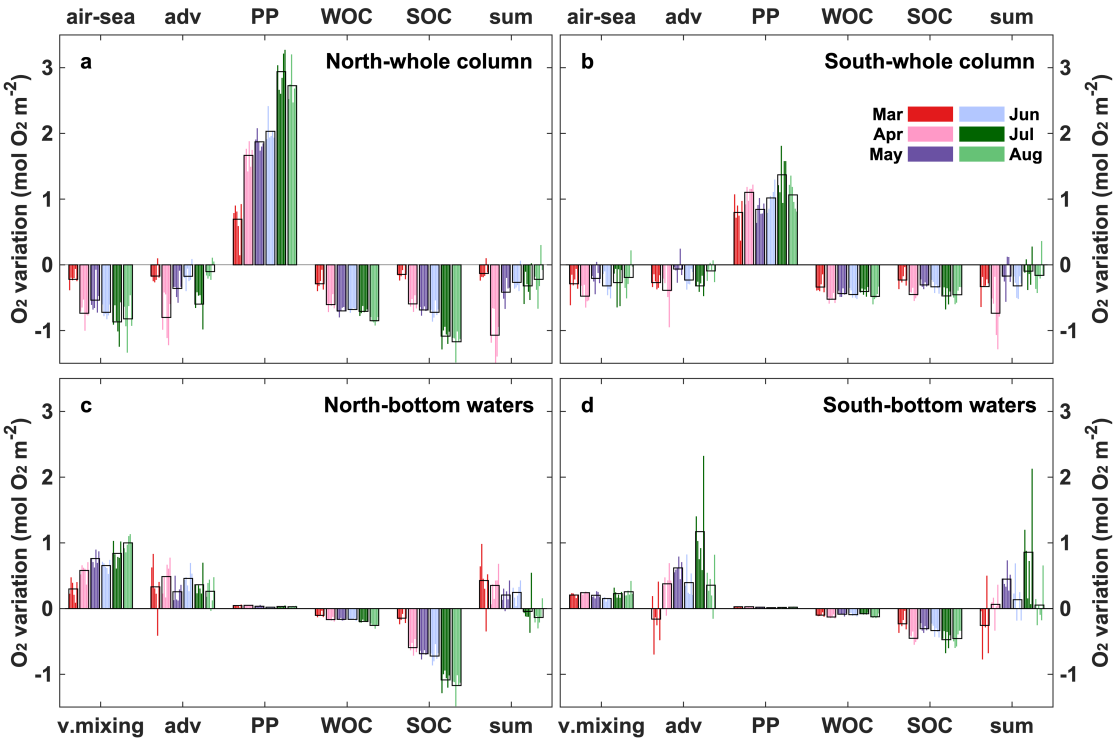

Figure 12. Monthly averaged (2008-2013) oxygen budgets for the whole water column and subsurface water from March to August in the northern and southern hypoxic regions. Adv represents lateral advection and lateral diffusion which is comparatively small, while v.mixing represents vertical turbulent diffusion, which is only relevant for the subsurface budget. Thin color bars represent individual years whereas the black bars are the 6-year average.

For the whole water column (Figure 12a, b), biological processes (PP, WOC, and SOC) greatly exceed physical processes (air-sea exchange and advective transport) in affecting oxygen. PP is always greater than the sum of WOC and SOC in the whole column indicating autotrophy in spring and summer. Advection is negative, acting as an oxygen sink and offsetting 21% of PP on average in the northern and southern regions. Of the two biological oxygen consumption terms (WOC and SOC), WOC accounts for half of total respiration. Negative air-sea flux indicates oxygen outgassing into the atmosphere and is due to photosynthetic oxygen production and decreasing oxygen solubility. However, since hypoxia only occurs in the subsurface, the subsurface budget below is more instructive.

When considering only subsurface waters (Figure 12c, d), the influence of PP decreases markedly, accounting for less than 2% of that in the whole water column. Vertical turbulent

diffusion acts as the largest oxygen source in the subsurface layer. SOC is the dominant oxygen sink accounting for 80% of the total biological oxygen consumption. As photosynthetic oxygen production increases gradually from spring to summer (Figure 12a, b) WOC and SOC also increase as they are closely associated with photosynthetically produced organic matter. Vertical oxygen diffusion tends to covary with PP, implying an oxygen gradient driven by photosynthetic oxygen production in the upper layer. Lateral advection of oxygen is negative in March only (early in the hypoxic season) mainly in the southern region, but becomes positive later. This suggests that early in the hypoxic season, import of low-oxygen water contributes to hypoxia generation but advection switches to an oxygen source later. Overall, oxygen sources and sink terms are similar in the northern and southern regions.

4. Discussion

We implemented and validated a state-of-the-art physical-biological model for the ECS. The implementation is based on a model that was previously developed and extensively used for the northern Gulf of Mexico (Fennel et al. 2011, Laurent et al. 2012, Yu at al.2015b), a region that is similar to the ECS in that it receives large inputs of FW and nutrients from a major river and develops extensive, annually recurring hypoxia (see Table 1 in Fennel and Testa (2019). Our model is more comprehensive than previous models for the ECS.

A 6-year simulation was performed and validated. The model faithfully represents patterns and variability in surface and bottom temperature and salinity, surface chlorophyll and nitrate distributions, bottom oxygen, and correctly simulates the major current patterns in the region (see Section 3.1 and Supplement). We thus deem the model's skill as sufficient for the analysis of biological and physical drivers of hypoxia generation presented here.

The model simulates annually recurring hypoxic conditions but with significant interannual and intra-seasonal variability and marked differences in phenology of hypoxic conditions from year to year (Figure 4a, b, c). Interannual variability in hypoxic conditions is much larger than variations in FW input, nutrient load, and bottom oxygen concentrations (Figure 4b) because small variations in oxygen can lead to large changes in

hypoxic area when bottom oxygen is near the hypoxic threshold. Interannual variability in hypoxic area is partly explained by variations in annual FW input, consistent with previous studies (Zheng et al., 2016; Zhou et al., 2017). While the correlation between time-integrated hypoxic area and FW input is insignificant, there is a strong and significant negative correlation between mean bottom oxygen in August and annual FW input (Figure 5). Annual FW input is also correlated strongly and significantly with the annually integrated spatial extent of the FW plume, which is a useful metric for extent of the region directly influenced by riverine inputs which induce strong density stratification and high productivity.

Surprisingly, DIN load is not correlated with FW input, hypoxic area, and mean bottom oxygen in August (Figure 5). This is in contrast to the northern Gulf of Mexico where DIN load is highly correlated with both FW input and nutrient load and frequently used as a predictor of hypoxic extent (Scavia et al. 2017, Laurent and Fennel 2019). However, the lack of correlation between hypoxia and DIN load in the ECS should not be interpreted as biological processes being unimportant in hypoxia generation, just that variations in DIN load do not explain year-to-year differences. In fact, hypoxic area and biological rates (i.e. mean August PP, OC, and SOC) are strongly and significantly correlated (Figure 5), emphasizing the dominant role of biological oxygen consumption. The fact that riverine variations in DIN load do not seem to have an effect suggests that riverine nutrient inputs are large enough to saturate the region with nutrients, similar to the northern Gulf of Mexico where small reductions in nutrient load have a relatively small effect (Fennel and Laurent 2018).

Variations in riverine FW input only partly explain interannual variations in hypoxia. For example, the years 2010 and 2012 had similar FW inputs and DIN loads but the hypoxic area was 4 times larger in 2010 than 2012 (Figure 5a). Similarly, 2009 and 2013 had the same FW inputs and nutrient loads but 2009 experienced extensive hypoxia while there was almost none in 2013. In order to elucidate these differences, we investigated biological and physical drivers of intra-seasonal variability.

In the ECS, two distinct zones of low oxygen have been observed (Li et al., 2002; Wei et al., 2007; Zhu et al., 2016, 2011). The model simulates these two zones, referred to as the northern and southern zone, consistent with observations (Figure 4d) and with generally

553 higher PP and SOC in the northern zone (Figure 6). Because of these differences we treated
554 the two zones separately in our analysis of intra-seasonal drivers.
555 We found daily biological rates (i.e. PP, OC, SOC) to be significantly correlated with
556 bottom oxygen in both zones, but with relatively large variability around the best linear fit
557 (Figure 7). The biological rates and bottom oxygen are also significantly correlated with
558 the extent of the FW plume (Table 1). Again, these results emphasize the dominant role of
559 biological oxygen consumption, and its relation to riverine inputs, in hypoxia generation
560 but leave a significant fraction of the variability unexplained.
561 We conducted an analysis of the effects of wind direction and strength on hypoxia. Wind
562 direction has a notable effect on the geographic distribution of hypoxia. Southerly,
563 upwelling-favorable winds lead to a more widespread eastward extension of the FW plume
564 with elevated PP and vertical density stratification (Figure 9). Northerly, downwelling-
565 favorable winds create a coastally trapped southward jet that moves FW southward and
566 constrains the plume close to the coast. A similar behavior has been described for the
567 northern Gulf of Mexico (Feng et al. 2014).
568 Wind strength turned out to be an important factor in hypoxia evolution. We identified
569 high-wind events and showed that whenever bottom oxygen is low, a high-wind event will
570 lead to a partial reoxygenation of bottom waters and decrease hypoxic extent (Figure 10).
571 The impact of high-wind events is also visible in the extent of the FW plume, which is
572 drastically reduced during high winds because FW is mixed. The frequency of high-wind
573 events during summer explains the differences in hypoxic area between 2010 and 2012
574 (Figure 11) and 2009 and 2013 (Figure S8). In 2009 and 2010 there were only few high-
575 wind events during summer while 2012 and 2013 experienced a sequence of storms that
576 led to partial reoxygenation of the water column throughout the summer and thus impeded
577 the development hypoxia.
578 We calculated oxygen budgets for the northern and southern regions considering the
579 whole water-column and the near-bottom layer only. The subsurface budget is particularly
580 useful in providing insights into when and where lateral advection amplifies or mitigates
581 hypoxia and illustrates that SOC is the dominant oxygen sink in the subsurface. The relative
582 importance of WOC and SOC had not previously been quantified for this region due to
583 lack of concurrent WOC and SOC observations and lack of models that realistically

account for both processes. The budget for the whole water column is less useful because it is dominated by the oxygen sources, sinks and transport in the surface layer, which does not experience hypoxia and thus is not relevant.

The importance of SOC in our model is consistent with recent observational studies in the ECS. SOC on the coastal shelves in the Yellow Sea and ECS has been estimated to range from 1.7 to 17.6 mmol O_2 m^{-2} d^{-1} (mean rate of 7.2 mmol O_2 m^{-2} d^{-1}) from April to October except August by Song et al. (2016), and from 9.1 to 62.5 mmol O_2 m^{-2} d^{-1} (mean of 22.6±16.4 mmol O_2 m^{-2} d^{-1}) from June to October in Zhang et al. (2017). Simulated SOC in the typical low-oxygen zone falls within the range observed by Zhang et al. (2017) with a mean rate of 20.6±19.2 mmol O_2 m^{-2} d^{-1} between April and October. Based on observations, Zhang et al. (2017) already suggested that SOC is a major contributor to hypoxia formation in below-pycnocline waters, which is further corroborated by our model results. It is also consistent with the modelling study of Zhou et al. (2017), who did not include SOC in the baseline version of their model but showed in a sensitivity study that inclusion of SOC simulates hypoxic extent more realistically. Our results are in line with findings from the northern Gulf of Mexico hypoxic zone where WOC is much larger than SOC below the pycnocline, while SOC is dominant in the bottom 5 m where hypoxia occurs most frequently in summer (Quiñones-Rivera et al., 2007; Yu et al., 2015b).

The finding that lateral oxygen transport can act as a net source to subsurface water is also new. On seasonal scales, oxygen advection in the subsurface varies from an oxygen sink in spring to a source in summer, especially in the southern hypoxic region, implying that the TWC becomes an oxygen source when oxygen is depleted in the hypoxic region. This aspect was neglected in previous studies which only emphasized the role of advection as an oxygen sink promoting hypoxia formation (Ning et al., 2011; Qian et al., 2015). The TWC originates from the subsurface of the Kuroshio northeast to Taiwan Island, and thus represents an intrusion onto the continental shelves from the open ocean (Guo et al., 2006). In addition to oxygen advection, nutrients are transported supporting primary production on the ECS shelves (Zhao & Guo, 2011, Grosse et al. 2020). The intrusion of the TWC and the Kuroshio accompanied by relatively cold and saline water, and nutrient and oxygen transport, is thought to influence hypoxia development (Li et al., 2002; Wang, 2009; Zhou

et al., 2017) but no quantification of the relative importance has occurred until now (see companion paper by Grosse et al., 2020, using the same model).

5. Conclusions

In this study, a new 3D coupled physical-biological model for the ECS was presented and used to explore the spatial and temporal evolution of hypoxia off the CE and to quantify the major processes controlling interannual and intra-seasonal oxygen dynamics. Validation shows that the model reproduces the observed spatial distribution and temporal evolution of physical and biological variables well.

A 6-year simulation with realistic forcing produced large interannual and intra-seasonal variability in hypoxic extent despite relatively modest variations in FW input and nutrient loads. The interannual variations are partly explained by variations in FW input but not DIN load. Nevertheless, elevated rates of biological oxygen consumption are of paramount importance for hypoxia generation in this region, as shown by the high correlation between hypoxic area, bottom oxygen, and biological rates (PP, OC, SOC) on both annual and shorter time scales.

Other important explanatory variables of variability in hypoxia are wind direction and strength. Wind direction affects the magnitude of PP and the spatial extent of the FW plume, because southerly, upwelling favorable winds tend to spread the plume over a large area while northerly, downwelling-favorable winds push the plume against the coast and induce a coastal current the contains the FW and moves it downcoast. Wind strength is important because high-wind events lead to a partial reoxygenation whenever bottom oxygen is low and can dramatically decrease the extent of the FW plume. The frequency of high-wind events explains some of the interannual differences in hypoxia, where years with similar FW input, nutrient load, and mean rates of oxygen consumption have display very different hypoxic extents because high-wind events lead to partial reoxygenation of bottom waters.

A model-derived oxygen budget shows that SOC is larger than WOC in the subsurface of the hypoxic region. Lateral advection of oxygen in the subsurface switches from an oxygen sink in spring to a source in summer especially in the southern region and is likely associated with open-ocean intrusions onto the coastal shelf supplied by the Taiwan Warm Current.

Acknowledgments: HZ was supported by the National Key Research and Development Program of China (2016YFC1401602 and 2017YFC1404403) and the China Scholarship Council (CSC). The authors thank the crew of the Dongfanghong2 for providing much help during the sampling cruises, and Compute Canada for access to supercomputer time. KF acknowledges support from the NSERC Discovery Program.

Code/Data Availability: The ROMS model code is available at http://myroms.org. NOAA AVHRR and MODIS-Terra are available at https://www.nodc.noaa.gov/SatelliteData/ghrsst/ and http://oceancolor.gsfc.nasa.gov/. The model results are available on request to the authors.

Author Contributions: The manuscript is based on HZ's PhD thesis (in Chinese). CB implemented the physical model. HZ added the biological component, performed model simulations, and wrote the first version of the manuscript with input from KF and AL. For the manuscript revision, AL reran the model simulation, AL and KF performed additional analyses, and KF revised the text with input from all co-authors.

Competing Interests: The authors declare they have no competing interests.

References

Baird, D., Christian, R. R., Peterson, C. H., & Johnson, G. A.: Consequences of hypoxia on estuarine ecosystem function: Energy diversion from consumers to microbes. Ecological Applications, 14(3), 805–822. https://doi.org/10.1890/02-5094, 2004.

Bian, C., Jiang, W., & Greatbatch, R. J.: An exploratory model study of sediment transport sources and deposits in the Bohai Sea, Yellow Sea, and East China Sea. Journal of Geophysical Research: Oceans, 118(11), 5908–5923. https://doi.org/10.1002/2013JC009116, 2013a.

Bian, C., Jiang, W., Quan, Q., Wang, T., Greatbatch, R. J., & Li, W.: Distributions of suspended sediment concentration in the Yellow Sea and the East China Sea based on field surveys during the four seasons of 2011. Journal of Marine Systems, *121–122*, 24–35, https://doi.org/10.1016/j.jmarsys.2013.03.013, 2013b.

Bianchi, T. S., DiMarco, S. F., Cowan, J. H., Hetland, R. D., Chapman, P., Day, J. W., & Allison, M. A.: The science of hypoxia in the northern Gulf of Mexico: A review. Science of the Total Environment, 408(7), 1471–1484. https://doi.org/10.1016/j.scitotenv.2009.11.047, 2010.

675 Bishop, M. J., Powers, S. P., Porter, H. J., & Peterson, C. H.: Benthic biological effects of
676 seasonal hypoxia in a eutrophic estuary predate rapid coastal development. Estuarine, Coastal
677 and Shelf Science, 70(3), 415–422. https://doi.org/10.1016/j.ecss.2006.06.031, 2006.
678 Capet, A., Beckers, J. M., & Grégoire, M.: Drivers, mechanisms and long-term variability of
679 seasonal hypoxia on the Black Sea northwestern shelf - Is there any recovery after
680 eutrophication? Biogeosciences, 10(6), 3943–3962. https://doi.org/10.5194/bg-10-3943-2013,
681 2013.
682 Carton, J. A., & Giese, B. S.: A Reanalysis of Ocean Climate Using Simple Ocean Data
683 Assimilation (SODA). Monthly Weather Review, 136(8), 2999–3017,
684 https://doi.org/10.1175/2007MWR1978.1, 2008.
685 Chen, C. C., Gong, G. C., & Shiah, F. K., Hypoxia in the East China Sea: One of the largest
686 coastal low-oxygen areas in the world. Marine Environmental Research, 64(4), 399–408.
687 https://doi.org/10.1016/j.marenvres.2007.01.007, 2007.
688 Chen, J., Cui, T., Ishizaka, J., & Lin, C.: A neural network model for remote sensing of diffuse
689 attenuation coefficient in global oceanic and coastal waters: Exemplifying the applicability of
690 the model to the coastal regions in Eastern China Seas. Remote Sensing of Environment, *148*,
691 168–177. https://doi.org/10.1016/j.rse.2014.02.019, 2014.
692 Chen, X., Shen, Z., Li, Y., & Yang, Y.: Physical controls of hypoxia in waters adjacent to the
693 Yangtze Estuary: A numerical modeling study. Marine Pollution Bulletin, *97*(1–2), 349–364.
694 https://doi.org/10.1016/j.marpolbul.2015.05.067, 2015a.
695 Chen, X., Shen, Z., Li, Y., & Yang, Y.: Tidal modulation of the hypoxia adjacent to the Yangtze
696 Estuary in summer. Marine Pollution Bulletin, *100*(1), 453–463,
697 https://doi.org/10.1016/j.marpolbul.2015.08.005, 2015b.
698 Dee, D. P., Uppala, S. M., Simmons, A. J., Berrisford, P., Poli, P., Kobayashi, S., … Vitart, F.:
699 The ERA-Interim reanalysis: Configuration and performance of the data assimilation system.
700 Quarterly Journal of the Royal Meteorological Society, *137*(656), 553–597.
701 https://doi.org/10.1002/qj.828, 2011.
702 Diaz, R. J., & Rosenberg, R.: Spreading dead zones and consequences for marine ecosystems.
703 Science, *321*(5891), 926–929. https://doi.org/10.1126/science.1156401, 2008.
704 Egbert, G. D., & Erofeeva, S. Y.: Efficient inverse modeling of barotropic ocean tides. Journal of
705 Atmospheric and Oceanic Technology, *19*(2), 183–204. https://doi.org/10.1175/1520-
706 0426(2002)019<0183:EIMOBO>2.0.CO;2, 2002.

Feng, Y., Fennel, K., Jackson, G.A., DiMarco, S.F. & Hetland, R.D.: A model study of the response of hypoxia to upwelling favorable wind on the northern Gulf of Mexico shelf, Journal of Marine Systems 131, 63-73, 2014.

Fennel, K., and Testa, J.M.: Biogeochemical controls on coastal hypoxia, Annual Review of Marine Science, 11, 105-130, https://doi.org/10.1146/annurev-marine-010318-095138, 2019.

Fennel, K. and Laurent, A.: N and P as ultimate and proximate limiting nutrients in the northern Gulf of Mexico: implications for hypoxia reduction strategies, Biogeosciences, 15, 3121-3131, https://doi.org/ /10.5194/bg-15-3121-2018, 2018.

Fennel, K., Hetland, R., Feng, Y., & DiMarco, S.: A coupled physical-biological model of the Northern Gulf of Mexico shelf: Model description, validation and analysis of phytoplankton variability. Biogeosciences, *8*(7), 1881–1899. https://doi.org/10.5194/bg-8-1881-2011, 2011.

Fennel, K., Hu, J., Laurent, A., Marta-Almeida, M., & Hetland, R.: Sensitivity of hypoxia predictions for the northern Gulf of Mexico to sediment oxygen consumption and model nesting. Journal of Geophysical Research: Oceans, *118*(2), 990–1002. https://doi.org/10.1002/jgrc.20077, 2013.

Fennel, K., Wilkin, J., Levin, J., Moisan, J., O'Reilly, J., & Haidvogel, D.: Nitrogen cycling in the Middle Atlantic Bight: Results from a three-dimensional model and implications for the North Atlantic nitrogen budget. Global Biogeochemical Cycles, *20*(3), 1–14. https://doi.org/10.1029/2005GB002456, 2006.

Garcia, H. E., Boyer, T. P., Locarnini, R. A., Antonov, J. I., Mishonov, A. V, Baranova, O. K., … Johnson, D. R.: World Ocean Atlas 2013. Volume 3: dissolved oxygen, apparent oxygen utilization, and oxygen saturation. NOAA Atlas NESDIS 75, 2013a.

Garcia, H. E., Locarnini, R. A., Boyer, T. P., Antonov, J. I., Baranova, O. K., Zweng, M. M., … Johnson, D. R.: World Ocean Atlas 2013, Volume 4 : Dissolved Inorganic Nutrients (phosphate, nitrate, silicate). NOAA Atlas NESDIS 76 (Vol. 4), 2013b.

Grosse, F., Fennel, K., Zhang, H., Laurent, A.: Quantifying the contributions of riverine vs. oceanic nitrogen to hypoxia in the East China Sea, Biogeosciences, https://doi.org/10.5194/bg-2019-342, accepted for publication

Guo, J. S., X. M. Hu and Y. L. Yuan: A diagnostic analysis of variations in volume transport through the Taiwan Strait using satellite altimeter data, Advances in Marine Science, 23(1): 20 – 26 (in Chinese with English abstract), 2005.

Haidvogel, D. B., Arango, H., Budgell, W. P., Cornuelle, B. D., Curchitser, E., Di Lorenzo, E., … Wilkin, J., Ocean forecasting in terrain-following coordinates: Formulation and skill

740 assessment of the Regional Ocean Modeling System. Journal of Computational Physics,
741 227(7), 3595–3624. https://doi.org/10.1016/j.jcp.2007.06.016, 2008.
742 Laurent, A., & Fennel, K.: Simulated reduction of hypoxia in the northern Gulf of Mexico due to
743 phosphorus limitation. Elementa: Science of the Anthropocene, *2*(1), 000022.
744 https://doi.org/10.12952/journal.elementa.000022, 2014.
745 Laurent, A., Fennel, K.: Time-evolving, spatially explicit forecasts of the northern Gulf of
746 Mexico hypoxic zone. Environmental Science & Technology, 53, 14,449-14,458, doi:
747 10.1021/acs.est.9b05790, 2019.
748 Laurent, A., Fennel, K., Hu, J., & Hetland, R.: Simulating the effects of phosphorus limitation in
749 the Mississippi and Atchafalaya river plumes. Biogeosciences, *9*(11), 4707–4723.
750 https://doi.org/10.5194/bg-9-4707-2012, 2012.
751 Laurent, A., Fennel, K., Cai, W.-J., Huang, W.-J., Barbero, L., Wanninkhof, R.: Eutrophication-
752 Induced Acidification of Coastal Waters in the Northern Gulf of Mexico: Insights into Origin
753 and Processes from a Coupled Physical-Biogeochemical Model. Geophys. Res. Lett., *44* (2),
754 946–956. https://doi.org/10.1002/2016GL071881, 2017.
755 Li, D., Zhang, J., Huang, D., Wu, Y., & Liang, J.: Oxygen depletion off the Changjiang (Yangtze
756 River) Estuary. Science in China Series D: Earth Science, *45*(12), 1137.
757 https://doi.org/10.1360/02yd9110, 2002.
758 Li, H. M., Tang, H. J., Shi, X. Y., Zhang, C. S., & Wang, X. L.: Increased nutrient loads from the
759 Changjiang (Yangtze) River have led to increased Harmful Algal Blooms. Harmful Algae, *39*,
760 92–101. https://doi.org/10.1016/j.hal.2014.07.002, 2014.
761 Li, M., Lee, Y. J., Testa, J. M., Li, Y., Ni, W., Kemp, W. M., & Di Toro, D. M.: What drives
762 interannual variability of hypoxia in Chesapeake Bay: Climate forcing versus nutrient loading?
763 Geophysical Research Letters, *43*(5), 2127–2134. https://doi.org/10.1002/2015GL067334,
764 2016.
765 Li, X., Bianchi, T. S., Yang, Z., Osterman, L. E., Allison, M. A., DiMarco, S. F., & Yang, G.:
766 Historical trends of hypoxia in Changjiang River estuary: Applications of chemical biomarkers
767 and microfossils. Journal of Marine Systems, *86*(3–4), 57–68, 2011.
768 https://doi.org/10.1016/j.jmarsys.2011.02.003
769 Liu, K. K., Yan, W., Lee, H. J., Chao, S. Y., Gong, G. C., & Yeh, T. Y.: Impacts of increasing
770 dissolved inorganic nitrogen discharged from Changjiang on primary production and seafloor
771 oxygen demand in the East China Sea from 1970 to 2002. *Journal of Marine Systems*, *141*,
772 200–217. https://doi.org/10.1016/j.jmarsys.2014.07.022, 2015.

773 Liu, S. M., Hong, G.-H., Ye, X. W., Zhang, J., & Jiang, X. L.: Nutrient budgets for large Chinese
774 estuaries and embayment. Biogeosciences Discussions, *6*(1), 391–435.
775 https://doi.org/10.5194/bgd-6-391-2009, 2009.
776 Liu, S. M., Zhang, J., Chen, H. T., Wu, Y., Xiong, H., & Zhang, Z. F.: Nutrients in the
777 Changjiang and its tributaries. Biogeochemistry, *62*(1), 1–18, 2003.
778 Locarnini, R. A., Mishonov, A. V., Antonov, J. I., Boyer, T. P., Garcia, H. E., Baranova, O.
779 K., … Seidov, D.: World Ocean Atlas 2013. Vol. 1: Temperature. S. Levitus, Ed.; A.
780 Mishonov, Technical Ed.; NOAA Atlas NESDIS, 73, 40. https://doi.org/10.1182/blood-2011-
781 06-357442, 2013.
782 Ni, X., Huang, D., Zeng, D., Zhang, T., Li, H., & Chen, J.: The impact of wind mixing on the
783 variation of bottom dissolved oxygen off the Changjiang Estuary during summer. Journal of
784 Marine Systems, 154, 122–130. https://doi.org/10.1016/j.jmarsys.2014.11.010, 2016.
785 Ning, X., Lin, C., Su, J., Liu, C., Hao, Q., & Le, F.: Long-term changes of dissolved oxygen,
786 hypoxia, and the responses of the ecosystems in the East China Sea from 1975 to 1995. Journal
787 of Oceanography, 67(1), 59–75. https://doi.org/10.1007/s10872-011-0006-7, 2011.
788 Peña, A., Katsev, S., Oguz, T., & Gilbert, D.: Modeling dissolved oxygen dynamics and hypoxia.
789 Biogeosciences, *7*(3), 933–957. https://doi.org/10.5194/bg-7-933-2010, 2010.
790 Qian, W., Dai, M., Xu, M., Kao, S. ji, Du, C., Liu, J., … Wang, L.: Non-local drivers of the
791 summer hypoxia in the East China Sea off the Changjiang Estuary. Estuarine, Coastal and
792 Shelf Science, 1–7. https://doi.org/10.1016/j.ecss.2016.08.032, 2015.
793 Quiñones-Rivera, Z. J., Wissel, B., Justić, D., & Fry, B.: Partitioning oxygen sources and sinks in
794 a stratified, eutrophic coastal ecosystem using stable oxygen isotopes. Marine Ecology
795 Progress Series, *342*, 69–83. https://doi.org/10.3354/meps342069, 2007.
796 Rabalais, N. N., Díaz, R. J., Levin, L. A., Turner, R. E., Gilbert, D., & Zhang, J.: Dynamics and
797 distribution of natural and human-caused hypoxia. Biogeosciences, *7*, 585–619.
798 https://doi.org/10.5194/bg-7-585-2010, 2010.
799 Scavia, D., Bertani, I., Obenour, D. R., Turner, R. E., Forrest, D. R. & Katin, A.: Ensemble
800 modeling informs hypoxia management in the northern Gulf of Mexico, P. Natl. Acad. Sci.
801 USA, 114, 8823–8828, 2017.
802 Scully, M. E.: Physical controls on hypoxia in Chesapeake Bay: A numerical modeling study.
803 Journal of Geophysical Research: Oceans, *118*(3), 1239–1256,
804 https://doi.org/10.1002/jgrc.20138, 2013.
805 Smolarkiewicz, P. K., & Margolin, L. G.: MPDATA: A finite-difference solver for geophysical
806 flows. Journal of Computational Physics, 140, 459-480, 1998.

807 Song, G., Liu, S., Zhu, Z., Zhai, W., Zhu, C., & Zhang, J.: Sediment oxygen consumption and
808 benthic organic carbon mineralization on the continental shelves of the East China Sea and the
809 Yellow Sea. Deep-Sea Research Part II: Topical Studies in Oceanography, *124*, 53–63.
810 https://doi.org/10.1016/j.dsr2.2015.04.012, 2016.
811 Tong, Y., Zhao, Y., Zhen, G., Chi, J., Liu, X., Lu, Y., … Zhang, W.: Nutrient Loads Flowing into
812 Coastal Waters from the Main Rivers of China (2006–2012). Scientific Reports, *5*, 16678.
813 https://doi.org/10.1038/srep16678, 2015.
814 Umlauf, L., & Burchard, H.: A generic length-scale equation for geophysical. Journal of Marine
815 Research, *61*(2), 235–265. https://doi.org/10.1357/002224003322005087, 2003.
816 Wang, B.: Hydromorphological mechanisms leading to hypoxia off the Changjiang estuary.
817 Marine Environmental Research, 67(1), 53–58,
818 https://doi.org/10.1016/j.marenvres.2008.11.001, 2009.
819 Wang, B., Wei, Q., Chen, J., & Xie, L.: Annual cycle of hypoxia off the Changjiang (Yangtze
820 River) Estuary. Marine Environmental Research, *77*, 1–5,
821 https://doi.org/10.1016/j.marenvres.2011.12.007, 2012.
822 Wang, B., Chen, J., Jin, H., Li, H., Huang, D., & Cai, W.-J.: Diatom bloom-derived bottom water
823 hypoxia off the Changjiang Estuary, with and without typhoon influence, Limnology and
824 Oceanography, 62, 1552-1569, https://doi.org/10.1002/lno.10517, 2017.
825 Wang, H., Dai, M., Liu, J., Kao, S. J., Zhang, C., Cai, W. J., … Sun, Z.: Eutrophication-Driven
826 Hypoxia in the East China Sea off the Changjiang Estuary. Environmental Science and
827 Technology, 50(5), 2255–2263. https://doi.org/10.1021/acs.est.5b06211, 2016.
828 Wang, J., Yan, W., Chen, N., Li, X., & Liu, L.: Modeled long-term changes of DIN:DIP ratio in
829 the Changjiang River in relation to Chl-α and DO concentrations in adjacent estuary. Estuarine,
830 Coastal and Shelf Science, *166*, 153–160. https://doi.org/10.1016/j.ecss.2014.11.028, 2015.
831 Wei, H., He, Y., Li, Q., Liu, Z., & Wang, H.: Summer hypoxia adjacent to the Changjiang
832 Estuary. Journal of Marine Systems, 67(3–4), 292–303,
833 https://doi.org/10.1016/j.jmarsys.2006.04.014, 2007.
834 Wei, H., Luo, X., Zhao, Y., & Zhao, L.: Intraseasonal variation in the salinity of the Yellow and
835 East China Seas in the summers of 2011, 2012, and 2013. Hydrobiologia, *754*(1), 13–28.
836 https://doi.org/10.1007/s10750-014-2133-9, 2015.
837 Wu, R. S. S.: Hypoxia: From molecular responses to ecosystem responses. Marine Pollution
838 Bulletin, *45*(1–12), 35–45. https://doi.org/10.1016/S0025-326X(02)00061-9, 2002.

Yu, L., Fennel, K., & Laurent, A.: A modeling study of physical controls on hypoxia generation in the northern Gulf of Mexico. Journal of Geophysical Research C: Oceans, *120*(7), 5019–5039. https://doi.org/10.1002/2014JC010634, 2015a.

Yu, L., Fennel, K., Laurent, A., Murrell, M. C., & Lehrter, J. C.: Numerical analysis of the primary processes controlling oxygen dynamics on the Louisiana shelf. Biogeosciences, *12*(7), 2063–2076. https://doi.org/10.5194/bg-12-2063-2015, 2015b.

Yuan, D., Zhu, J., Li, C., & Hu, D.: Cross-shelf circulation in the Yellow and East China Seas indicated by MODIS satellite observations. Journal of Marine Systems, *70*(1–2), 134–149. https://doi.org/10.1016/j.jmarsys.2007.04.002, 2008.

Zhang, H., Zhao, L., Sun, Y., Wang, J., & Wei, H.: Contribution of sediment oxygen demand to hypoxia development off the Changjiang Estuary. Estuarine, Coastal and Shelf Science, 192, 149–157. https://doi.org/10.1016/j.ecss.2017.05.006, 2017.

Zhang, J.: Nutrient elements in large Chinese estuaries. Continental Shelf Research, *16*(8), 1023–1045. https://doi.org/10.1016/0278-4343(95)00055-0, 1996.

Zhao, L., & Guo, X.: Influence of cross-shelf water transport on nutrients and phytoplankton in the East China Sea: A model study. Ocean Science, *7*(1), 27–43. https://doi.org/10.5194/os-7-27-2011, 2011.

Zheng, J., Gao, S., Liu, G., Wang, H., & Zhu, X.: Modeling the impact of river discharge and wind on the hypoxia off Yangtze Estuary. Natural Hazards and Earth System Sciences, 16(12), 2559–2576. https://doi.org/10.5194/nhess-16-2559-2016, 2016.

Zhou, F., Chai, F., Huang, D., Xue, H., Chen, J., Xiu, P., … Wang, K.: Investigation of hypoxia off the Changjiang Estuary using a coupled model of ROMS-CoSiNE. Progress in Oceanography, 159, 237–254. https://doi.org/10.1016/j.pocean.2017.10.008, 2017.

Zhou, F., Huang, D., Ni, X., Xuan, J., Zhang, J., & Zhu, K.: Hydrographic analysis on the multi-time scale variability of hypoxia adjacent to the Changjiang River Estuary. Shengtai Xuebao/ Acta Ecologica Sinica, 30(17), 4728–4740, 2010.

Zhu, J., Zhu, Z., Lin, J., Wu, H., & Zhang, J.: Distribution of hypoxia and pycnocline off the Changjiang Estuary, China. Journal of Marine Systems, *154*, 28–40. https://doi.org/10.1016/j.jmarsys.2015.05.002, 2016.

Zhu, Z.-Y., Zhang, J., Wu, Y., Zhang, Y.-Y., Lin, J., & Liu, S.-M.: Hypoxia off the Changjiang (Yangtze River) Estuary: Oxygen depletion and organic matter decomposition. *Marine Chemistry*, *125*(1–4), 108–116. https://doi.org/10.1016/j.marchem.2011.03.005, 2011.

871 Zweng, M. M., Reagan, J. R., Antonov, J. I., Mishonov, A. V., Boyer, T. P., Garcia, H. E., …
872 Bidlle, M. M., World Ocean Atlas 2013, Volume 2: Salinity. NOAA Atlas NESDIS (Vol. 119).
873 https://doi.org/10.1182/blood-2011-06-357442, 2013.
874